Scalable three-dimensional hybrid continuum-discrete multiscale modeling of granular media

Weijian Liang[1] | Huanran Wu[2] | Shiwei Zhao[3,4] | Wei Zhou[5] | Jidong Zhao*[1,5]

[1]Department of Civil and Environmental Engineering, Hong Kong University of Science and Technology, Clearwater Bay, Kowloon, Hong Kong, China
[2]School of Civil Engineering, Chongqing University, Chongqing 400045, China
[3]State Key Laboratory of Subtropical Building Science, South China University of Technology, Guangzhou, China
[4]South China Institute of Geotechnical Engineering, South China University of Technology, Guangzhou, China
[5]State Key Laboratory of Water Resources and Hydropower Engineering Science, Wuhan University, China

Correspondence
*Jidong Zhao, Dept. of Civil and Environmental Engineering, Hong Kong University of Science and Technology, Clear Water Way, Kowloon, Hong Kong SAR.
Email: jzhao@ust.hk

Abstract

This study presents a scalable three-dimensional (3D) multiscale framework for continuum-discrete modeling of granular materials. The proposed framework features rigorous coupling of a continuum-based Material Point Method (MPM) and a discrete approach Discrete Element Method (DEM) to enable cross-scale modeling of boundary value problems pertaining to granular media. It employs MPM to solve the governing equations of a macroscopic continuum domain for a boundary value problem that may undergo large deformation. The required loading-path-dependent constitutive responses at each material point of the MPM are provided by a DEM solution based on grain-scale contact-based discrete simulations that receive macroscopic information at the specific material point as boundary conditions. This hierarchical coupling enables direct dialogues between the macro and micro scales of granular media while fully harnessing the predictive advantages of both MPM and DEM at the two scales. An effective, scalable parallel scheme is further developed, based on the flat Message Passing Interface (MPI) model, to address the computational cost of the proposed framework for 3D large-scale simulations. We demonstrate that the proposed parallel scheme may offer up to 32X and 40X speedup in strong and weak scaling tests, respectively, significantly empowering the numerical performance and predictive capability of the proposed framework. The 3D parallelized multiscale framework is validated by an element test and a column collapse problem, before being applied to simulating the intrusion of a solid object. The multiscale simulation successfully captures the characteristic response of intrusion as postulated by the modified Archimedes' law theory. The progressive development of the stagnant zone during the intrusion is further examined from a cross-scale perspective.

KEYWORDS:
multiscale simulation, MPM, DEM, parallel computing, large deformation, intruder

1 | INTRODUCTION

Granular media exist in diversified forms pertaining to engineering fields and industries, including geomaterials (including sand, gravel, and rock), snow, food grains, mining products, chemical powders, and pharmaceutical tablets. The behavior of

This article has been accepted for publication and undergone full peer review but has not been through the copyediting, typesetting, pagination and proofreading process which may lead to differences between this version and the Version of Record. Please cite this article as doi: 10.1002/nme.6963

granular media is important to these various sectors, but is well regarded among the most challenging ones to understand. They may exhibit properties of both solid and liquid and undergo transitions between two. As typical porous media, their behavior may be further complicated by interstitial liquid or gas or a mixture of them. A concerted effort has been paid across many disciplines in an attempt to gain a better scientific understanding of specific or common features of granular media. In civil engineering, for example, advanced constitutive models and theories have been established to model the mechanical response of granular soils under various loading conditions, including the renowned Mohr-Coulomb failure criterion, the stress dilatancy theories[1], critical state soil mechanics[2,3,4], and the anisotropic critical state theory (ACST)[5,6]. Various theories have been developed in cryosphere science to describe the behavior of snow or glacial ice[7,8] and their phase transition[9,10,11]. These theories and models have greatly transformed our understanding on granular media specialized in various loading conditions and engineering circumstances. It remains a challenge, however, to develop a general theory or predictive model that may describe many complicated aspects of granular media responses (such as anisotropy[12], liquefaction and strain localization[13]) under a wide range of different loading conditions (including monotonic, cyclic and rotational shear loading[14]) and deformation/flow regimes (small strain, large deformation, and flow).

The complexity of mechanical responses of granular material has its grain-scale origin. External loads may mobilize rich inter-granular interactions at the particle level of a granular body, presenting in forms of inter-particle friction, sliding, rolling, and others to establish force transmissions and deformation fields. Macroscopic phenomena are often collective manifests of these grain-scale mechanisms. Accurate understanding and rigorous prediction of the behavior of granular media have to take into account the grain-scale physics and mechanics where conventional continuum-based theories prove to be inadequate. Hierarchical multiscale modeling represents an emerging recent thrust of research in computational mechanics that attempts to bridge key grain-scale interactions and mechanisms with macroscopically observed phenomena via computational modeling. To this end, the multiscale modeling approach typically employs a hierarchical structure that couples a continuum and a discrete-based methods in providing cross-scale solutions. In treating granular media, for example, Discrete Element Method (DEM) has commonly been used to to provide particle-based micromechanics solution for one of the following continuum approaches, such as MPM[15], FEM[16,17,18,19,20], or Smooth Particle Finite Element Method (SPFEM)[21]. The hierarchical coupling helps to circumvent the use of phenomenological constitutive laws and enables cross-scale analysis. These approaches have demonstrated great potential in modeling various engineering applications, *e.g.*, compaction band in high-porosity sandstones[22,23,24], pull-out of anchors[25] and foundations over anisotropic soil[26].

This study aims to tackle a series of correlated challenges that prevent the further advance of this multiscale approach, namely, 3D simulations of large deformation and failure problems as well as the incurred computational cost. First, almost all existing studies on hierarchical multiscale modeling of granular media have been two-dimensional (2D) due to various reasons, expensive computational cost being one of them. Although 2D simulations can indeed capture the key features for a wide range of engineering problems, they remain idealized simplifications that cannot offer adequate characterizations of real-world problems. Specifically, existing 2D studies commonly use discs (2D) in DEM to represent granular grains, and prohibit all out-of-plane grain motions and inter-particle interactions. Though such a setting may still render qualitatively sound predictions of the behavior of granular media[27], the predictions may not be quantitatively comparable against experimental data (*e.g.*, porosity, peak/residual stress, and dilatancy). It is also well-known that macroscopic phenomena of granular media are affected not only by the mechanical properties of specimens but also by the geometry setting and the loading conditions. A representative case is the compression test on the sand. For a densely-packed sample, cross-shaped shear bands are commonly observed under a plane strain setting, whereas octopus-shaped shear localization zone and diffuse failure may occur under triaxial compression or extension[28]. Indeed, in the setting of a boundary value problem, material points at different locations of a problem may well undergo different loading conditions. To capture the influence of loading conditions on the failure behavior, 3D modeling is required. Moreover, the 2D setting may also prevent modeling of some practical problems with realistic topography[29,30]. Therefore a true 3D multiscale modeling framework is highly desirable. Second, though the extension from 2D to 3D is conceptually straightforward, it remains challenging from an implementation perspective. A crucial issue to be addressed for 3D multiscale modeling is to mitigate the tremendous computational cost involved. Taking the MPM-DEM multiscale modeling as an example, for a typical 3D problem, the amount of material points involved is at least one order of magnitude larger than that in 2D. The RVE is embedded in each material point also needs to have more grain particles in the DEM solver in 3D than 2D. These two factors interplay in a multiplying manner in increasing the demand for computational resources, causing several order of magnitude increase in computational cost for 3D modeling as compared to its 2D counterpart. It is mandatory that a high-performance solution has to be developed to make 3D multiscale approach entirely feasible for practical simulation.

This study aims to propose a three-dimensional (3D) framework for continuum-discrete modeling of granular media to ease the limitations of existing 2D approaches. To accommodate the enormous computational cost of 3D multiscale modeling, we propose a scalable and efficient parallel scheme for accelerating the computation. We further port the integrated modeling framework into a high-performance supercomputer facility (Tianhe-2) for large-scale computations. The rest of the paper is organized as follows. The 3D MPM-DEM multiscale framework is firstly introduced in Section 2. Section 3 elaborates the proposed parallel scheme and its implementation. Numerical examples, including a unit element test, a column collapse simulation, and the intrusion of a solid object, are presented and discussed in Section 4. Section 5 finally concludes this study with major findings and some further work.

2 | METHODOLOGY: HIERARCHICAL CONTINUUM-DISCRETE COUPLING

The multiscale framework in this study is established through a hierarchical coupling of a continuum method MPM and a discrete method DEM. The MPM is used to solve a macroscopic boundary value problem (BVP) that may undergo large deformation. Attached to each material point of the MPM is a DEM assembly to serve a Representative Volume Element (RVE). The RVE receives boundary conditions from its attached material point to provide history-dependent mechanical responses for MPM through grain-scale, contact-based DEM simulations. The two-way, two-scale information passing helps to avoid assuming phenomenological constitutive models in solving large deformation problems. The 2D concept has been introduced in our previous work [15]. For sake of completeness, the following presents a brief recap of the hierarchical modeling framework emphasizing the general 3D case.

2.1 | MPM solver

The kinematics and deformation of a continuum are assumed to be governed by the following the conservation of mass and momentum:

$$\frac{\mathrm{D}\rho}{\mathrm{D}t} = 0 \tag{1}$$

$$\rho\frac{\mathrm{D}\mathbf{v}}{\mathrm{D}t} = \nabla\cdot\boldsymbol{\sigma} + \rho\mathbf{g} \tag{2}$$

where ρ is the density; $\mathbf{v}$ denotes the velocity; $\boldsymbol{\sigma}$ is the Cauchy stress tensor and $\mathbf{g}$ is the gravity. In MPM, the continuum domain is discretized into a number of Lagrangian points (material point) which carry the mass, momentum, and other internal variables, e.g., stress $\boldsymbol{\sigma}$, deformation gradient $\boldsymbol{F}$ and void ratio e. Since these material points retain their mass throughout the computation, the mass conservation is automatically satisfied. To facilitate the computation of the spatial derivatives, MPM adopts an Eulerian grid as its background mesh, allowing the mapping of information from the material points to the grid nodes and vice versa. Moreover, with the background mesh as a scratch pad, the aforementioned momentum conservation can be derived in following weak form:

$$\dot{\boldsymbol{p}}_I = \boldsymbol{f}_I^{int} + \boldsymbol{f}_I^{ext} \tag{3}$$

with

$$\dot{\boldsymbol{p}}_I = \sum_p \dot{\boldsymbol{p}}_p S_{Ip} \tag{4}$$

$$\boldsymbol{f}_I^{int} = -\sum_p \boldsymbol{\sigma}_p\cdot\nabla S_{Ip} V_p \tag{5}$$

$$\boldsymbol{f}_I^{ext} = \sum_p m_p \boldsymbol{b} S_{Ip} + \int_{\partial\Omega} N_I \boldsymbol{\tau}\, dS \tag{6}$$

where the subscript 'p' and 'I' denote the properties associated with material point and grid node, respectively; $\dot{\boldsymbol{p}}_I$ is the material time derivative of nodal momentum; $\boldsymbol{f}_I^{int}$ and $\boldsymbol{f}_I^{ext}$ are the internal and external nodal forces, respectively; $\dot{\boldsymbol{p}}_p$ is the material time derivative of momentum for material points; $\boldsymbol{\sigma}_p$ is the Cauchy stress; V_p and m_p are the volume and mass of the material point, respectively; $\boldsymbol{\tau}$ is the boundary traction; N_I is the shape function; S_{Ip} and ∇S_{Ip} are the weighting function and its gradient, respectively [31]. Once the nodal forces are computed, they are further distributed to its surrounding material points to update their states.

With the nature of conventional continuum-based method, MPM relies on a constitutive model to link deformation and stress. However, granular media are high nonlinear and history-dependent due to their discrete nature. Phenomenological models for granular media have gained certain success in specific loading conditions, *e.g.*, monotonic loading of pure rotational shear, it remains challenging for a single model (with one set of calibrated model parameters) to capture more complicated material response such as strain localization[13], anisotropy[12,6] and liquefaction under complex loading conditions such as general dynamic loading[14] as in earthquake. DEM has been proven to be versatile and robust in reproducing highly nonlinear response of granular media under different loading conditions, directly from an assembly of particles. Using DEM to replace the use of conventional constitutive models in MPM can not only preserve the discrete nature of granular media but also bypass the need for phenomenological assumptions. The hierarchical coupling of MPM with DEM is hereby a perfect match for granular media modeling.

2.2 | DEM Solver

DEM provides a numerical solution to each RVE attached to a material point in MPM for each incremental deformation at the macroscopic BVP. In DEM, the normal contact force $\boldsymbol{f}_n$ and tangential/shear contact force $\boldsymbol{f}_t$ are computed as follows:

$$\boldsymbol{f}_n = -k_n^c \delta \boldsymbol{n} \tag{7}$$

$$\boldsymbol{f}_t = -\min(k_t^c u_t, \boldsymbol{f}_n \tan\varphi)\boldsymbol{t} \tag{8}$$

where k_n^c and k_t^c are normal and tangential contact stiffness, respectively; δ is the contact overlap; u_t is the relative shear incremental displacement; φ is the inter-particle friction angle, and $\boldsymbol{n}$ and $\boldsymbol{t}$ are the unit normal vector and unit tangential vector of the contact, respectively.

In DEM simulation, two models, *i.e.*, the linear spring model and the Hertz-Mindlin contact model[32,33] are commonly used to describe the interaction between two contacted particles. The linear spring model assumes the contact stiffnesses to be constant, while the latter considers these stiffnesses varying with the contact overlap. It has been found that both models yield similar results on both microscopic and macroscopic mechanical behaviors of granular materials[34]. In our study, the linear spring model is adopted due to its computational efficient. In the linear spring model, the contact stiffnesses (k_n^c, k_t^c) are given by:

$$k_n^c = Er^* \tag{9}$$

$$k_t^c = \nu Er^* \tag{10}$$

where E is the Young's modulus; $r^* = 2r_i r_j/(r_i + r_j)$ is the harmonic mean of radii of the contacting particles; $\nu = k_t^c/k_n^c$ is the stiffness ratio. Note that rolling resistance is not considered in the current study.

In the proposed MPM-DEM framework, the essential information retrieved from the DEM solver is the Cauchy stress tensor $\boldsymbol{\sigma}$, which can be obtained by homogenizing over the deformed RVE based on Love-Weber formula[35,36]:

$$\boldsymbol{\sigma} = \frac{1}{V}\sum_{N_c} \boldsymbol{d} \otimes \boldsymbol{f}^c \tag{11}$$

where "$\otimes$" denotes the dyadic product; V is the total volume of the assembly; N_c is the whole contact inside the RVE; $\boldsymbol{d}$ is the branch vector joining centers of the contacting particles, and $\boldsymbol{f}^c$ is the contact force. Given the homogenized stress, the mean stress p and the deviatoric stress q can be defined as:

$$p = \frac{1}{3}\mathrm{tr}(\boldsymbol{\sigma}) \tag{12}$$

$$q = \sqrt{\frac{3}{2}\boldsymbol{s} : \boldsymbol{s}} \tag{13}$$

where "tr" indicates the trace of a tensor; ":" is the double contraction operator; $\boldsymbol{s} = \boldsymbol{\sigma} - p\boldsymbol{I}$ is the deviatoric part of the stress tensor $\boldsymbol{\sigma}$, and $\boldsymbol{I}$ is an identity tensor. Likewise, the volumetric strain ε_v is calculated as follows:

$$\varepsilon_v = \mathrm{tr}(\boldsymbol{\varepsilon}) = -\ln\frac{V_0}{V} \tag{14}$$

where $\boldsymbol{\varepsilon}$ is the strain tensor; V are the volume of RVE and V_0 is its initial value. Positive volumetric strain denotes dilatancy.

Averaged particle rotation θ is another quantity that could be extracted from RVE to examine the micro-mechanical behavior of granular media, which is given by:

$$\theta = \frac{1}{N}\sum_{N}\theta_p \tag{15}$$

where N is the number of DEM particle in a RVE; θ_p is the accumulated rotation of an individual particle inside the assembly.

3 | HIGH-EFFICIENCY PARALLEL SCHEME AND ITS IMPLEMENTATION FOR COUPLED MPM-DEM

The MPM-DEM multiscale framework comprises two simulation components: the macroscopic MPM solver handling the motion and deformation of the continuum body, and the mesoscopic DEM solver providing mechanical material responses based on particle-scale solutions. In particular, two popular open-source codes, `CB-Geo MPM`[37,38] and `YADE`[39] are employed for the MPM and DEM solvers, respectively.

To integrate these two modules for granular media modeling, a specified interface is required for two-way information exchanging of the deformation and mechanical response. As computational cost may be a concern, the interface engine should also accommodate potential high-performance computing schemes for multiscale computation. In this study, the interface engine has been designed as a coupler to serve as an external executable to manage the overall workflow of the simulation. Both the MPM and DEM solvers are attached to the coupler as libraries. The coupler is programmed in `Python` to facilitate code integration. This coupler has also been so designed to be sufficiently general and adaptable for other functionality enrichments, e.g., adopting specialized `SudoDEM`[26,40] for considering particle morphology. The implementation has been made noninvasive and user-friendly to avoid detailed refactoring for both solvers when it only needs to bind several `C++` functions to `Python` to link with the coupler. Part of the code will be made publicly available.

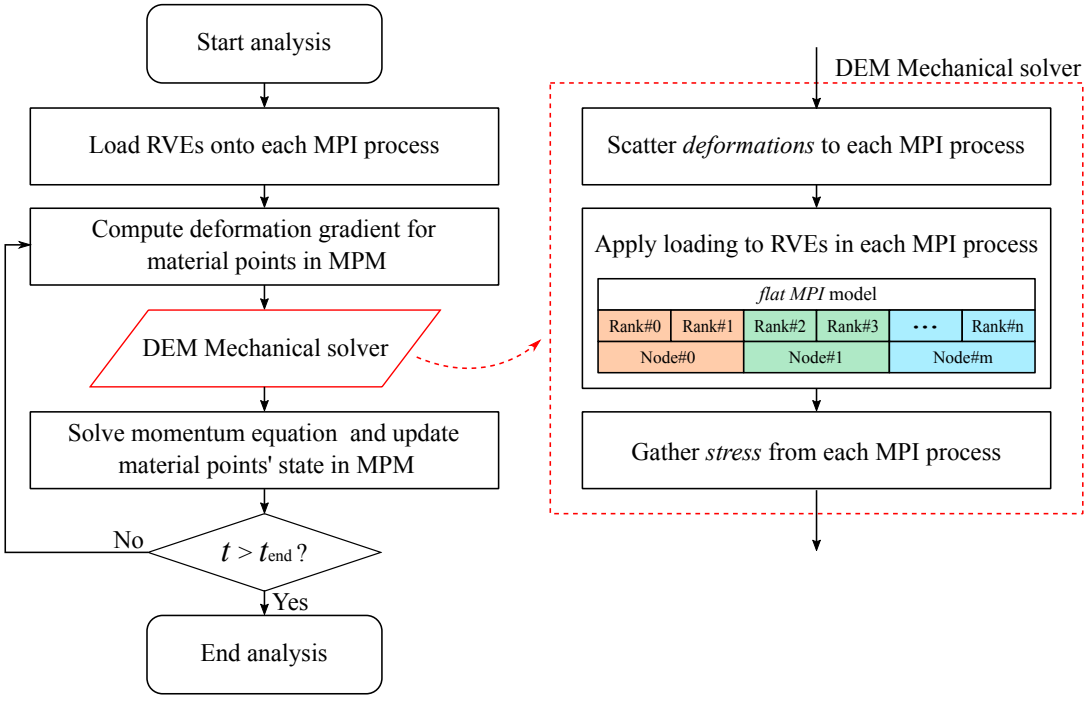

FIGURE 1 The workflow for the proposed MPM-DEM multiscale framework. Also shown is a schematic for *flat MPI* model in the DEM mechanical solver in which separate single-threaded MPI processes are executed on each core of cluster nodes.

Algorithm 1 Pseudocode for parallel MPM-DEM approach

```
if t = 0 then
    if rank = 0 then
        // In master MPI process
        MPM.initialization()
    end if
    MPI.Scatterv(rve_index)
    // In each MPI process
    for i in rve_index segment do
        DEM.addScene()
        DEM.loadRve(i)
    end for
end if
while 0 < t < t_end do
    if rank = 0 then
        MPM.computeDeformation()
    end if
    MPI.Scatterv(rve_deformation)
    // In each MPI process
    for i in rve_index segment do
        DEM.switchToScene(i)
        DEM.shearRve()
        DEM.computeStress()
    end for
    MPI.Gatherv(rve_stress)
    if rank = 0 then
        MPM.updateParticleState()
    end if
    t = t + Δt
end while
```

The workflow and the implementation for the parallel MPM-DEM multiscale framework are illustrated in Fig. 1 and Algorithm 1, respectively. Since the DEM simulation is the most computationally expensive part of the entire multiscale modeling, we have implemented the large-scale parallelization in distributed high-performance computing nodes based on Message Passing Interface (MPI) to accelerate this part solely, while leaving the less intensive MPM computation handled among different threads within a single node using `Intel`® oneAPI Threading Building Blocks (oneTBB)[41] for simplicity. In what follows, emphasis is placed upon the large-scale parallel computing scheme for DEM and we will use parallel scheme to denote this inter-node parallelization unless stated otherwise.

`Python` package `mpi4py` is exploited for implementation of the parallel scheme. This implementation is based on the single-level *flat MPI* model, in which separate single-threaded MPI processes are executed on each core of multiple nodes[42]. Prior to the explicit time integration, the MPM solver will undertake the task of initialization, including parsing the input file and creating the background mesh. At this stage, a number of MPI processes are launched by the coupler with each running an independent DEM solver. The set containing the entire RVEs/material points index is then divided nearly evenly into 'n' partitions ('n' is the amount of MPI process) which are distributed to all MPI processes. With the assigned index, DEM solver on each MPI process will load the corresponding RVE packings into local memory. It is noted that loading packing into separated processing unit helps to achieve data parallelism, minimizing subsequent data exchange between the master and slave processes, and hence reducing communication overhead.

Similar operations are executed in subsequent coupling cycles. First, the incremental displacement gradients $\mathrm{d}\boldsymbol{H}_p^{t+1}$ for all RVEs are computed in the MPM solver:

$$\text{from particle to grid:} \quad m_I^t = \sum_p S_{Ip} m_p, \quad \boldsymbol{p}_I^t = \sum_p S_{Ip} \boldsymbol{p}_p^t, \quad \boldsymbol{v}_I^t = \boldsymbol{p}_I^t / m_I^t \tag{16}$$

$$\text{from grid to particle:} \quad \mathrm{d}\boldsymbol{H}_p^{t+1} = \Delta t \sum_I \nabla S_{Ip} \boldsymbol{v}_I^t \tag{17}$$

where m_I^t, $\boldsymbol{p}_I^t$ and $\boldsymbol{v}_I^t$ represent mass, momentum and velocity at grid node I, respectively; m_p, $\boldsymbol{p}_p^t$ and $\boldsymbol{v}_p^t$ denote the mass, momentum and velocity of material point p, respectively. S_{Ip} and ∇S_{Ip} are the shape function and its gradient. The computed incremental displacement gradients ($\mathrm{d}\boldsymbol{H}_p^{t+1}$) are then distributed to all MPI processes by a collective communication routine `MPI.Scatterv()`. Based on these deformation information, the task of shearing RVE, which is the most computationally intensive part within the entire workflow, is undertaken by multiple DEM solvers held in different MPI processes. Once the loading of RVE is accomplished across all processing units, the material responses, *e.g.*, Cauchy stress (Eqn. 11), and averaged particle angular velocity (Eqn. 15), are retrieved from the deformed RVE and sent back to the master rank (via `MPI.Gatherv()`) to allow MPM solver to solve the momentum equation at grid node (Eqn. 3 - 6). Finally, with the updated grid node variables, the velocity $\boldsymbol{v}_p$ and position $\boldsymbol{x}_p$ for material points in MPM can be updated accordingly:

$$\boldsymbol{v}_p^{t+1} = \boldsymbol{v}_p^t + \Delta t \sum_I S_{Ip} \dot{\boldsymbol{p}}_I^{t+1} / m_I^t \tag{18}$$

$$\boldsymbol{x}_p^{t+1} = \boldsymbol{x}_p^t + \Delta t \sum_I S_{Ip} \boldsymbol{v}_I^{t+1}. \tag{19}$$

Another commonly used parallel scheme is the multi-level hybrid parallel model[43] in which coarse-grain parallelization is realized through MPI communication across nodes while fine-grain parallelization is achieved via loop-level parallelism inside each node using compiler optimizations such as OpenMP[44]. Although this hybrid MPI-OpenMP model may reduce the communication overhead over flat MPI model due to its allowing each thread directly access the shared memory within the same node, such performance enhancement may not compensate its complex programming. It is important to note that in the hierarchical multiscale framework, each RVE is independent of the others and thus only two collective communications, *i.e.*, `MPI.Scatterv()` and `MPI.Gatherv()`, are required in each computation step as shown in Algorithm 1. This favorable feature leads to a considerably low communication overhead as compared to those achieving parallelization via domain decomposition that requires frequent exchange of data for halo region (region shared between sub-domains).

Load balancing is also one of the key aspects for achieving an optimal parallel performance. In the present parallelism implementation, dynamic load balancing during runtime is not applicable, since RVEs are bound to specified MPI process before the main loop. Therefore, it is necessary to determine an optimal workload for assigned resources. One efficient and straightforward approach is randomly numbering material points during the pre-processing, so that RVE with different deformation could be distributed evenly, and consequently, each MPI process could handle a DEM task with similar computational intensity (note that the computational speed of DEM solver is slightly affected by the configuration of an RVE, *e.g.*, shearing a regular RVE is slightly faster than a skewed one). Such techniques are employed throughout this work.

The proposed 3D multiscale framework implemented with the above parallel schemes has further been ported to Tianhe-2, the National Supercomputer Center in Guangzhou, China (NSCC-GZ) for large-scale 3D simulations. Tianhe-2 has around 16,000 nodes with each equipped with 2-way 12-core Intel Xeon E5-2692v2 CPU, 3x Intel Xeon Phi co-processor and 64GB memory. It is also customized with internal high-speed interconnection TH-2 Express-2 within a torus network. Notably, although the proposed framework is run on massively large-scale architectures such as Tianhe-2, it is also suitable for medium-size clusters and common desktops since it is developed for the standard Linux environment, constrained only by the accessible memory.

4 | NUMERICAL EXAMPLES

Numerical examples are presented in this section for three-fold purposes: (1) to validate the accuracy of the overall three-dimensional MPM-DEM framework, (2) to examine the performance of the proposed parallel scheme, and (3) to demonstrate the predictive capability of the multiscale approach empowered by efficient parallelism for engineering problems pertaining to granular media. A number of problems with increasing complexity have been selected, from a simple unit element test to the

intrusion of solid objects into granular matter, to verify the accuracy, efficiency and versatility of the proposed 3D multiscale approach.

4.1 | Unit element test

Unit element test is useful for validating the accuracy of numerical approaches including both FEM and MPM (see [16,18,15]). We herein use the unit element test to verify the accuracy of the overall three-dimensional framework including the information passing scheme between the macroscale and mesoscale under diverse boundary conditions. The configuration of the problem is shown in Fig. 2 . The cube sample has an element size of 1 m, the vertical displacement for bottom surface is fixed, the lateral surfaces are subjected to surface tractions $\bar{\boldsymbol{t}} = 100$kPa and top surface is subjected to displacement loading Δu. The element is loaded to a state with a axial strain of $\varepsilon_{yy} = 50\%$ to validate the accuracy of the apporach at finite strain level. The unit cell comprises eight material points witch each attaching to an identical RVE. The RVE is generated with the following typical microscopic parameters: number of DEM particle $N = 800$, grain density $\rho = 2650\text{kg/m}^3$, radii of spherical particles r range from 3 to 7 mm ($\bar{r} = 5$ mm), Young's modulus $E = 100$MPa, stiffness ratio $\nu = k_t/k_n = 0.8$, and inter-particle friction $\mu = 0.5$. Each RVE packing is consolidated to a medium-dense initial state with a porosity $n = 0.373$ and a confining pressure $p_c = 100$kPa prior to the global loading. It is noteworthy that the number of DEM particles we use in each RVE is slightly smaller than those in [28,17] as our trail test show that the generated RVE also offer representative responses.

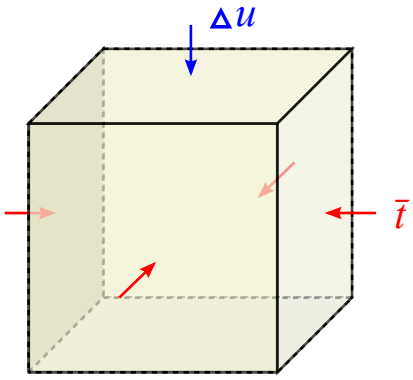

FIGURE 2 Model setup for the unit element test. The vertical displacement for bottom surface is fixed, the lateral surfaces are subjected to surface tractions $\bar{\boldsymbol{t}}$ and top one is subjected to displacement loading Δu.

Fig. 3 compares the MPM-DEM multiscale solutions, in terms of the stress-strain response and the dilatancy curve, with pure DEM simulations under the same loading condition of the unit test. It is evident that the multiscale solutions and pure DEM simulations consistently capture both the pre-peak and the strain softening responses and the dilatancy characteristics of the granular sample, confirming that the multiscale framework is well benchmarked. Note that the pure DEM simulations exhibit mild fluctuations due to the limited number of particles used for the RVE for intended computational efficiency.

4.2 | Granular column collapse

Three-dimensional granular column collapse has been frequently investigated in both experiments [45,46,47] and numerical simulations [47,48,49,50], which can be used as another benchmark test for the proposed framework. During the collapse process, the soil may simultaneously exhibit solid-like and fluid-like characteristics, making it challenging to predict by a single constitutive model. We hereby present a multiscale prediction of the column collapse problem and benchmark it with experimental test [46], to showcase the potential of MPM-DEM approach in capturing material response across both static and dynamics regimes. A series of scaling tests are further conducted to evaluate the performance of the proposed parallel scheme.

The model setup for the simulation shown in Fig. 4 follows exactly its experimental counterpart outlined in [46]. The initial height and length of granular column are set as $H_i = 60$mm and $L_i = 100$mm, respectively, with an aspect ratio of $a = H_i/L_i = 0.6$. The dimension of the final deposition are measured by H_f and L_f. The granular column is placed on a rectangular chamber

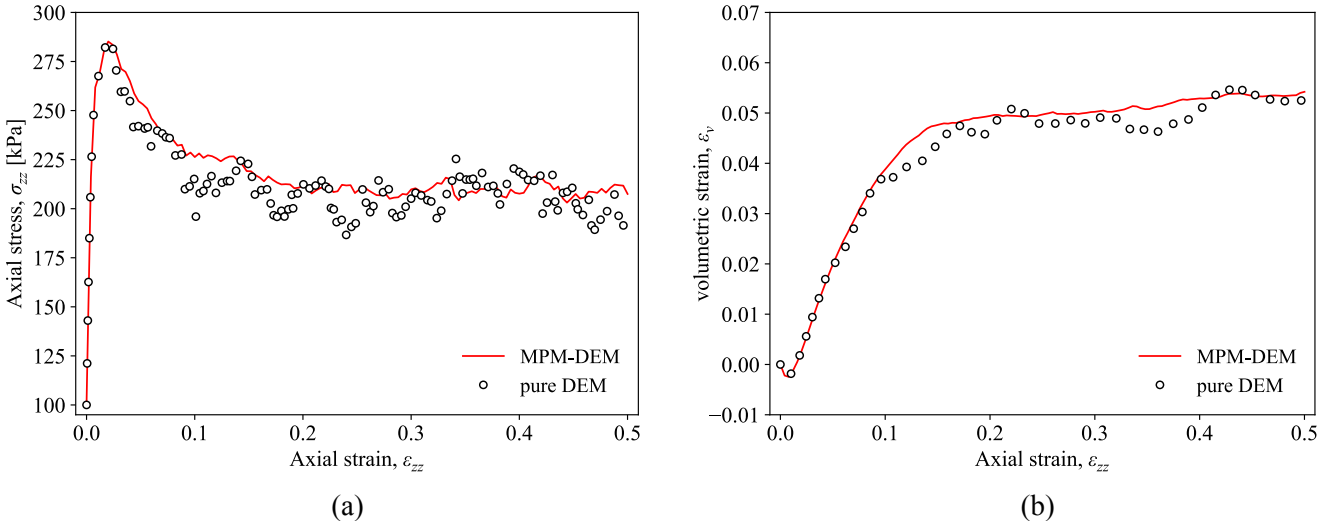

FIGURE 3 Benchmark of multiscale predictions by pure DEM simulations: stress response and dilatancy curve for the unit element test

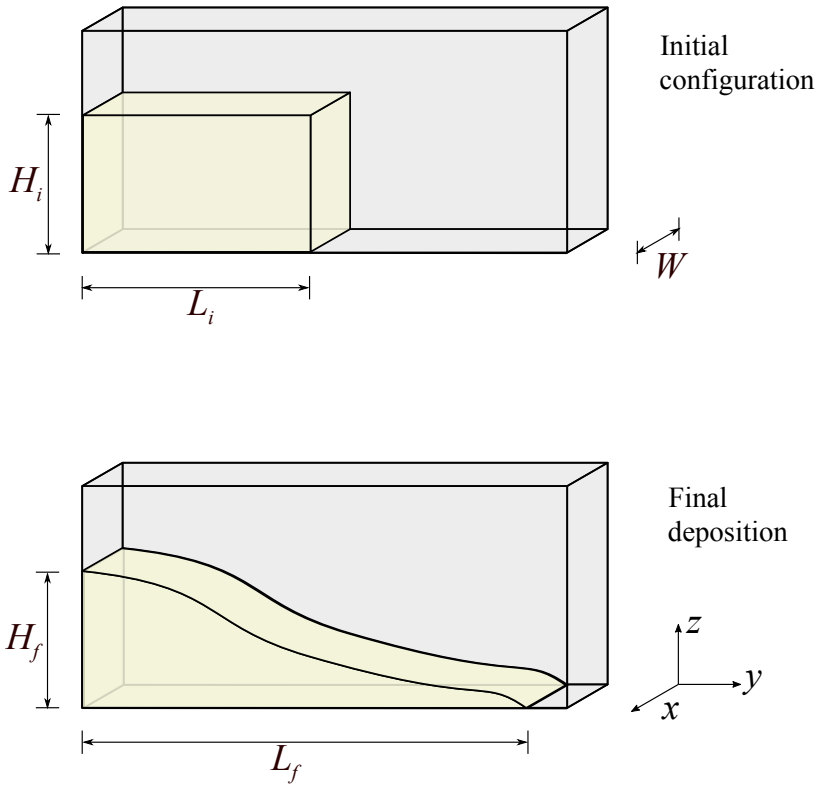

FIGURE 4 Model setup for the 3D column collapse problem

with a width of $W = 45$mm. The microscopic parameters for the RVEs are selected as: number of DEM particle $N = 800$, grain density $\rho = 2500\text{kg/m}^3$, radii of spherical particles $r = 1.8 \sim 4.2$mm ($\bar{r} = 3$ mm), Young's modulus $E = 600$MPa, stiffness ratio $\nu = k_t/k_n = 0.5$, inter-particle friction $\mu = 0.384$, and initial porosity $n = 0.401$. Specifically, the key parameter inter-particle friction μ is determined according to the experiment[46]. In this simulation, the bottom surface is assumed to be nonslip whereas the side walls are frictionless. Before the collapse is triggered, an additional Dirichlet boundary condition

(displacement constraint in y direction) is imposed at the outer lateral surface of the column to achieve an equilibrium stress state. This constraint is then removed to allow the column freely collapse and flow down. Following the experiment[46], a dimensionless characteristic time τ_c is adopted in the analysis, which is related to the free fall of the granular column via $\tau_c = \sqrt{H_i / g}$, where g is the gravity. Accordingly, the characteristic time herein is computed as $\tau_c = 0.0782s$, and $t = 0$ denotes the commencement of collapse process.

4.2.1 | Flow patterns

Fig. 5 shows a comparison of the velocity field obtained by our simulation and the experimental data from[46]. It is evident that the slumping initiates from the upper edge of the outer surface of the column. The whole column is divided into two distinct portions by a clear failure surface above which the soil slides down as almost an intact bulk mass while the lower part remains still. The development of the collapse process is so swift that at $t = 3\tau_c$, the majority of the soil ceases to move except the portion in the vicinity of the front and that close to the surface. The collapse process nearly ends $t = 7\tau_c$ as indicated by the extremely low velocity magnitude. Fig. 6 , further presents a quantitative comparison of the numerical predictions and the experimental measurements[46] in terms of the scaled distance traveled by the collapsing mass. Again, the multiscale simulation yields a good agreement with the experimental study despite a slight delay in the collapse evolution.

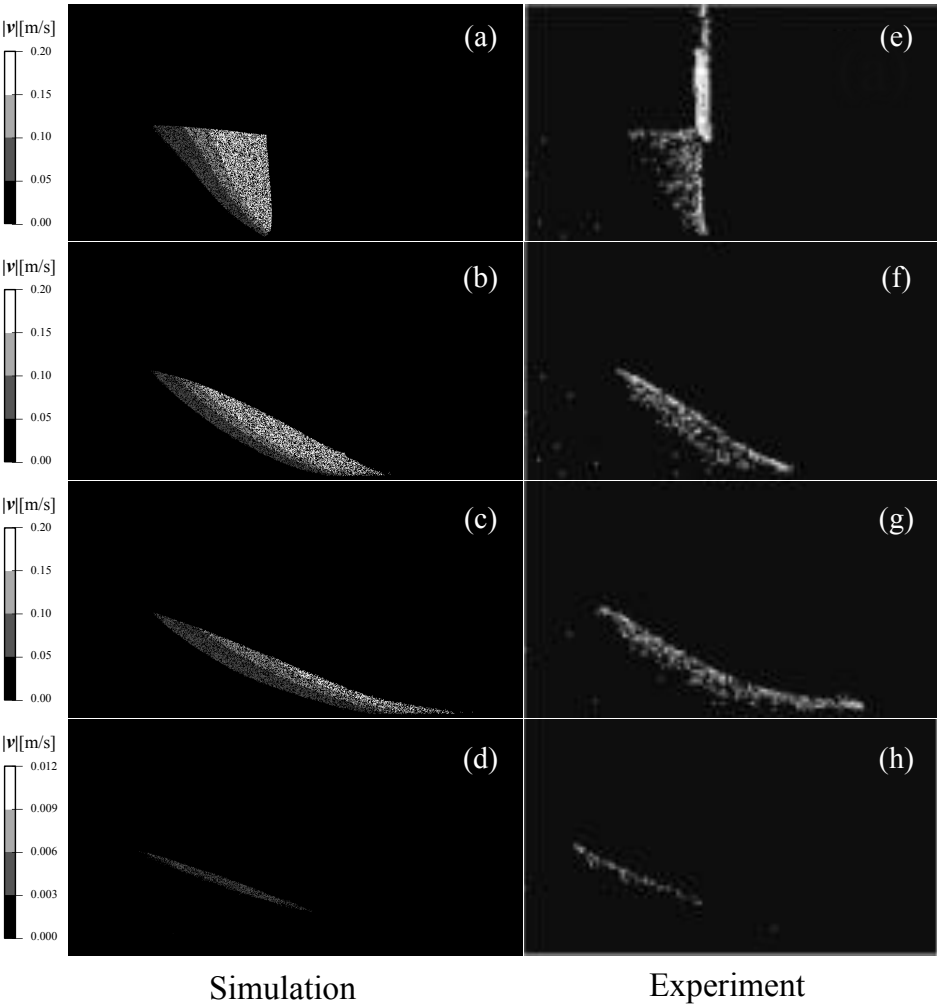

FIGURE 5 Snapshots (front view) of velocity field obtained from the simulation and experiment[46] at $t = 0.5\tau_c, 2\tau_c, 3\tau_c$ and $7\tau_c$.

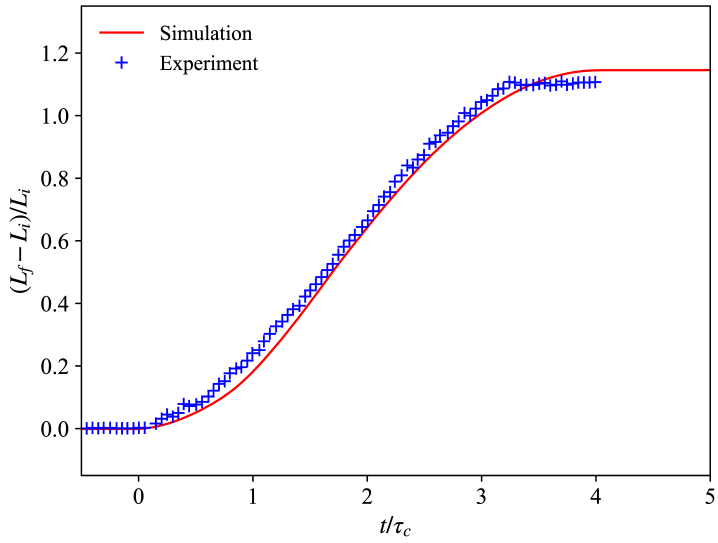

FIGURE 6 Scaled travelling distance of the collapsing mass (experimental data from[46])

4.2.2 | Parallelism performance: strong scaling

To evaluate the scalability and numerical performance of the proposed parallel scheme, a series of scaling tests are performed. We firstly examine the strong scaling test which is commonly used to measure the parallel efficiency for fixed workload problems (*i.e.*, fixed number of material points/RVEs). In this test, the granular column has the same geometry as the aforementioned one and consists of 50, 000 RVEs. The simulation runs 100 steps with varying number of computers (which we refer to as node(s) hereafter). While the number of steps is relatively small, it has a minor influence on the drawn conclusion since the explicit integration used in both MPM and DEM solvers renders a stable computational time in each step. To obtain a detailed profile for analyzing the runtime behavior of the multiscale framework, the elapsed time for MPM, DEM and MPI communication are recorded separately. In particular, the cost of MPM computing includes locating material points in the background mesh, computing deformation gradient for all RVEs, and updating momentums and positions of material points; the DEM cost refers to the time for shearing all RVEs; and the cost of MPI comprises scattering the deformation information and gathering homogenized stresses from all MPI process. Note that the file I/O routine (*e.g.*, output `.vtk` file) is not included in the scaling test since it is only called every thousand steps in typical practice. The strong scaling test is performed with 1 to 420 computing nodes (corresponding CPU cores ranging from 24 to 10, 080), leading to a patch size (number of RVE per MPI process) roughly varying from 2083 to 5. Due to constraints by memory, the scaling test with one node is conducted in the same system with a larger memory (128 GB).

For the strong scaling test, the average running time per step for each part of the simulation is shown in Fig. 7 . For the test without applying the parallel computing across multiple nodes, each DEM solution takes over 10 seconds, accounting for more than 97.7% of the overall elapsed time. It is thus reasonable to improve this specified part instead of the whole framework. Utilizing more nodes, it can be seen that the cost of the DEM drops substantially, approaching ideally to be inversely proportional to the number of nodes. On the other hand, as the MPM computation does not invoke any MPI-based parallelization, its consuming time stably varies between 0.27 s and 0.37 s. As for the MPI part, the communication overhead is comparatively low, around two orders of magnitude lower than that of the MPM part when the node number is small, *i.e.* smaller than 32. As more computing nodes are involved, the MPI cost increases dramatically. For example, the MPI overhead is around half of that of DEM when using 128 nodes. However, this communication overhead becomes one order higher than the latter when using 420 nodes, and gradually becomes the bottleneck of the multiscale simulation. While not presented for brevity, we also observed the communication overhead of scattering the incremental displacement gradient is slightly higher than that of gathering the stresses due to the former has larger message size.

With the running time profile, it is straightforward to measure the performance of the parallelism. It is noted that, we use the computational cost with 1 computer node (24 CPU cores) as our scaling reference as our focus is placed on the inter-node

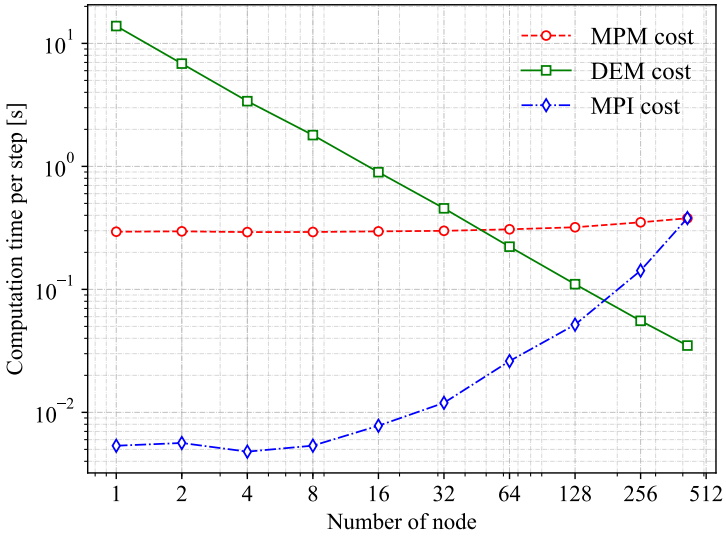

FIGURE 7 Averaged execution time per step for each part of the computation in the strong scaling test

parallelization. Herein, 'speedup' and 'parallel efficiency' are used to quantify the scalability and the efficiency of the proposed parallel scheme, which could be straightforwardly defined as:

$$\text{speedup} = t_1/t_{N_{node}} \tag{20}$$

$$\text{parallel efficiency} = t_1/(t_{N_{node}} \times N_{node}) \tag{21}$$

$$\tag{22}$$

where t_1 and $t_{N_{node}}$ denote the time needed to accomplish the computation using 1 and N_{node} node(s), respectively. In strong scaling test in parallel computing, the upper limit of speedup prescribed by Amdahl's law[51] reads:

$$\text{speedup} = \frac{1}{s + p/N_{node}} \tag{23}$$

where s is the fraction of serial part of the computation not amenable to parallelization referring to the MPM computational cost herein, while p is the proportion of parallelized computation. According to aforementioned time profile, p and s are taken as 0.977 and 0.023, respectively.

Fig. 8 (a) depicts the speedup for the overall computation (MPM + DEM + MPI) and DEM standalone parts. It can be seen that the DEM achieves an ideally linear enhancement of performance for all running configurations due to the independence of RVE with no communication overhead, demonstrating the efficiency of the proposed parallelism strategy. However, as for the overall performance, the speedup appears to approach the upper limit (Eq. 23) for the medium nodes size (*e.g.*, 128 nodes), and drops slightly with more nodes. Such a performance degradation is more noticeable in the parallel efficiency shown in Fig. 8 (b), especially when the node number increases from 32 to 128. Clearly, this reduction of efficiency is attributed to the exponential increase in communication overhead which overwhelms the performance enhancement pertaining to DEM. Fig. 8 , revealing that the proposed parallelism scheme based on flat MPI model is suitable for medium node size (*e.g.*, 64), and the bottlenecks in communication overhead eventually arise for larger node size and prevent the scheme from achieving an efficient scaling. For an extremely large number of nodes, devising more advanced multi-level parallelization may reduce the communication overhead and help leverage the strong scaling performance, which is, however, out of the scope of this work.

4.2.3 | Parallelism performance: weak scaling

A weak scaling test is also conducted to investigate the scalability of the parallelism. It is designed to examine whether the size of problems can be scaled up with the amount of available computational resources, which is of great importance in designing

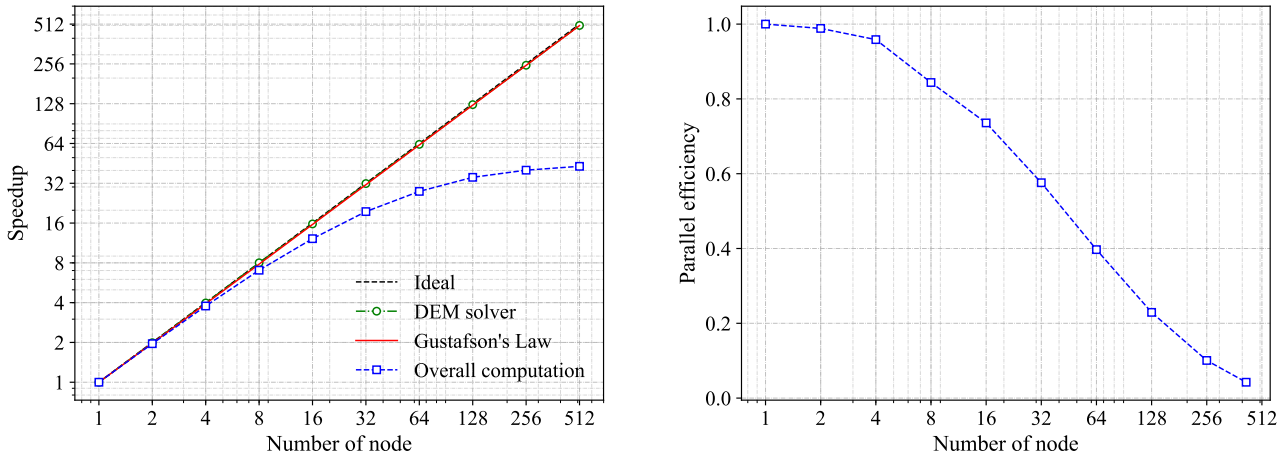

FIGURE 8 The parallel performance in the strong scaling test: (a) speedup, (b) parallel efficiency

the model setup. The simulation with 1 computer node is taken as the reference test which contains 4.800 RVEs. While other model systems increase by a factor of 2 in the problem size. The fully running configuration on Tianhe-2 invokes up to 512 nodes and 12, 288 CPU cores, resulting in a problem size of 2, 457, 600 RVEs which is at least two orders of magnitude larger than our previous multiscale simulations [15,52].

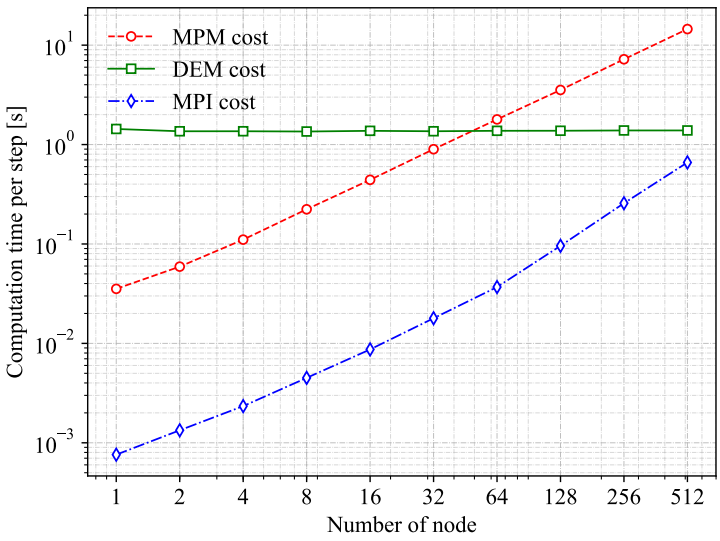

FIGURE 9 Averaged execution time per step for each part of the computation in the weak scaling test

Fig. 9 presents running time profile of the scaling test. It is evident that the DEM cost in each step stabilizes at around 1.3 s for different problem sizes. This is not surprising since the problem size is linearly proportional to the amount of nodes and the patch size (number of RVE per MPI process) remains constant during the course of scaling. In contrast, without implementing any MPI-based parallelism among distributed nodes, the MPM cost increases with the problem size and eventually exceeds the DEM part when the scaling factor is up to 64 (307, 200 RVEs). Likewise, the cost of MPI part also increases with the amount

of MPI processes, but remains approximately two orders lower than that of MPM. It is also noted that the increasing rate of MPI communication overhead appears to be faster once the node number is larger than 64, indicating a growing complexity of message communication with a larger number of MPI processes[53]. Similarly, we use 'scaled speedup' and 'parallel efficiency' for measuring the performance of parallelization in weak scaling, which could be defined as:

$$\text{scaled speedup} = t_1/t_{N_{node}} \times N_{node} \tag{24}$$

$$\text{parallel efficiency} = t_1/t_{N_{node}} \tag{25}$$

where N_{node} is incorporated in the scaled speedup to reflect different problems size involved. In weak scaling test of parallel computing, Gustafson's Law[54] provides an estimation of the upper bound of scaled speedup, which reads:

$$\text{scaled speedup} = s + p \times N_{node} \tag{26}$$

where s and p have the same definition as those in Eq. 23.

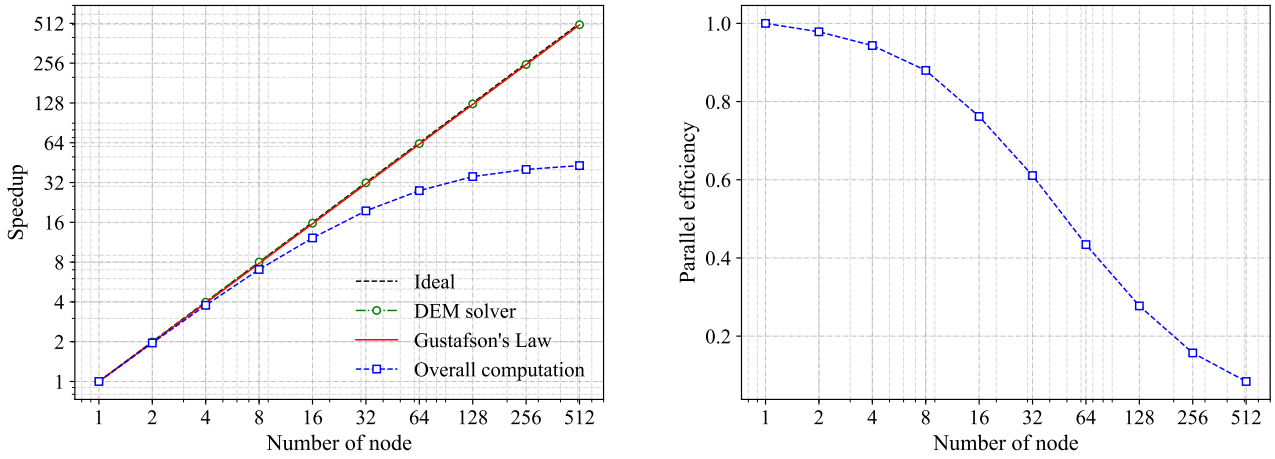

FIGURE 10 The parallel performance in the weak scaling test: (a) scaled speedup, (b) parallel efficiency

The parallel performance in the weak scaling test is plotted in Fig. 10 . Again, the parallel scheme manifests itself as the DEM computation, the kernel component of the multiscale framework, achieves almost ideal performance enhancement. Because of the relatively high value of p ($p = 0.977$), the bound obtained from Gustafson's Law[54] nearly converges to the ideal linear curve. The overall scaled speedup exhibits an almost linear increase when the node size is smaller than 64, where the problem has been enlarged up to 307, 200 RVEs. However, with the increase in both node size and the problem size, the parallel efficiency drops gradually and goes below 0.2 when the number of node increase to 256. Moreover, it is also observed that the scaled speedup diverges from Gustafson's Law prediction and reached only 40 at the fully running configuration. Clearly, this deviation is attributed to the characteristic of our parallel scheme which only implements MPI-based parallel computing on distributed nodes for the DEM part while the MPM computation is handled on a single node. Although this strategy is straightforward and efficient, it can hardly guarantee an optimal load balance. As shown in this weak scaling test (c.f. Fig. 9), when the problem size and node size are sufficiently large, the DEM computational task is accomplished as fast as or even faster than that of the MPM part, resulting in the occurrence of process idling and inevitable performance degradation. Though one could further improve the overall performance via implementing MPI-based parallelism for the MPM solver, it requires more advanced coding skills.

4.3 | Intrusion of solid object

The multiscale modeling framework empowered by the proposed parallel scheme renders it possible for efficient simulation of large-scale boundary value problems. A demonstration is presented on its simulation of the intrusion of a solid object into the granular media. Motivated by a recent study by[55], where the drag forces are examined experimentally by driving the intruder quasi-statically into the granular matter, *e.g.*, glass beads, quartz and millet. The same topic has attracted a series of interesting studies recently[56,10,57,58].

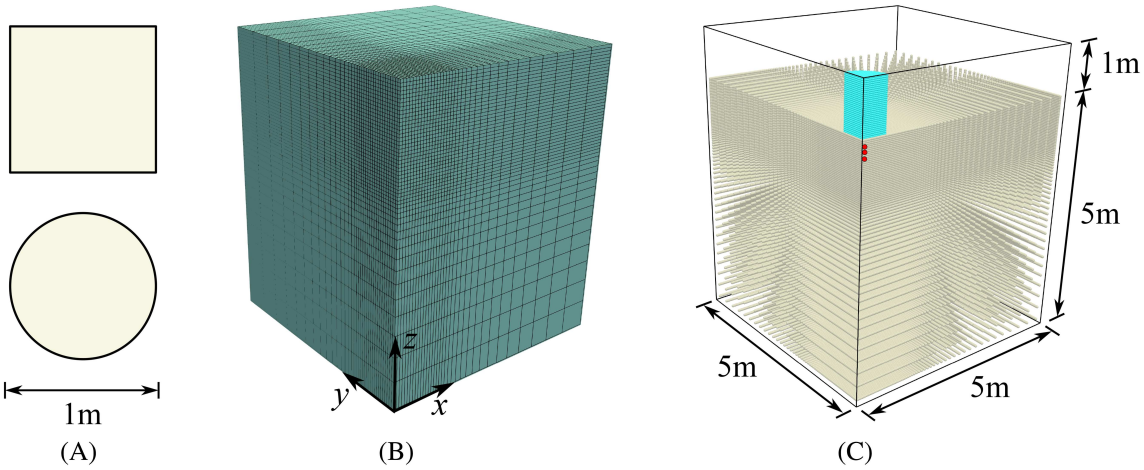

FIGURE 11 Model setup for the intrusion of solid object into granular media: (a) rectangular and circular cross-sections of the intruders (b) the background mesh and (c) the material points used to discretize the intruder and the soil

Fig. 11 illustrates the simulation setup involving two types of intruders with a dimension of 1 meter in both height and diameter: cylinder and cuboid. Given the symmetry nature of the problem, only one quarter of the domain is simulated with a dimension of $5 \times 5 \times 5$ m. Fig. 11 (b) and (c) show the mesh and the associated material points, respectively. The minimum element/cell has a size of 0.0625 m in each dimension, and each cell comprises 8 material points. During the simulation, the intrusion velocity first linearly increases to 0.25 m/s, and is then kept constant to alleviate the stress oscillation caused by the potential dynamic effect. Note that the selected loading velocity is sufficiently small to maintain a quasi-static penetration. Without losing generality, the RVEs are prepared with typical microscopic parameters that have the same values as those in the unit element test (Section 4.1). The initial porosity n of the RVE is around 0.397. In this example, the problem size allows a total simulation of up to $287,496$ RVEs and equivalently $229,996,800$ DEM particles. Each simulation takes around 39.6 hours to accomplish on 40 nodes (960 CPU cores).

We firstly investigate the deformation patterns of the granular media during the intrusion. Fig. 12 shows the displacement fields for both cases of cylindrical and the cuboid intruders. Despite the difference in the cross-section shape, both simulations share a similar deformation pattern: a cone-shaped stagnant zone is developed ahead of the intruders, displacing aside the frontal soils and penetrating downward alongside the intruders. As the penetration proceeds, the soil immediately on the side of the intruder is squeezed upwards, forming a mild heave on the ground surface. Since the soil used in the simulation is in a medium-dense state and does not exhibit apparent dilatancy, such heaving is insignificant. Also, it can be seen that the influencing region of the cuboid intruder, *i.e.*, the stagnant zone and the mobilized mass, is slightly larger than that of the cylindrical intruder because of the larger cross-section area.

Fig. 13 presents the vertical resistant force during the intrusion. In particular, dimensionless quantities, *i.e.*, normalized force $\widetilde{p}_u = p_u/(\rho g R)$ and normalized displacement $\widetilde{d} = d/R$, are introduced according to[55]. For the cuboid intruder, the equivalent radius $R_e = \sqrt{4S/\pi}$ is taken, where S is the area of intruder cross-section and the constant 4 accounts for the quarter model adopted. Fig. 13 shows that the $\widetilde{p}_u - \widetilde{d}$ relation for intruders with different cross-section shapes collapses to a single curve consisting of an initial nonlinear regime and a steady-state linear regime, in excellent agreement with the experimental observation[55,57]. Following past studies[55,57], we then fit this force-depth relation in steady regime by $\widetilde{p}_u = K_\phi \widetilde{d} + \widetilde{p}_0$. It is clear that the linear law fits the normalized forces of both intruders well with a gradient K_ϕ of 23.024. As pointed out in the recently

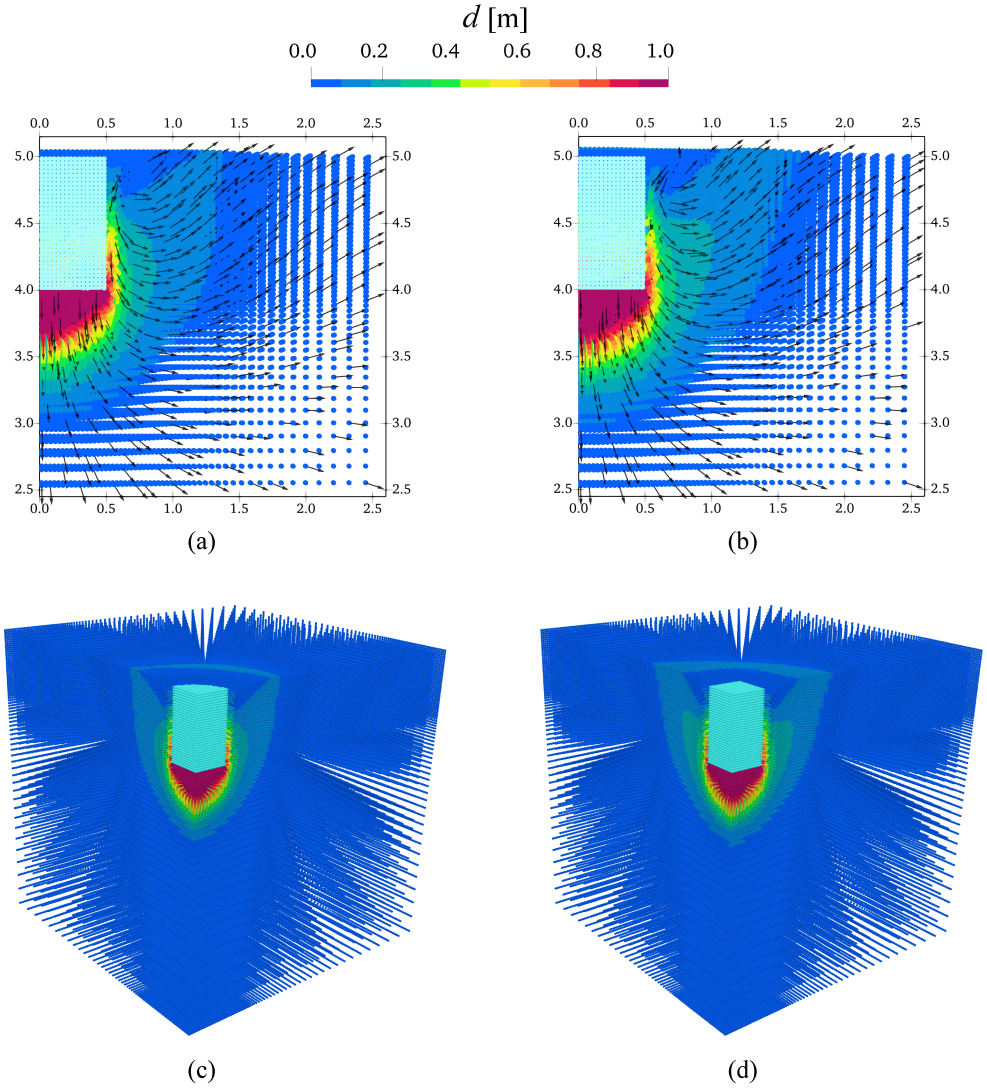

FIGURE 12 Contours of displacements for (a, c) cylindrical and (b, d) cuboid intruders at the final state

proposed modified Archimedes' law[55], K_ϕ is independent of the intruder shape. Instead, it depends only on the internal friction angle (repose angle) ϕ of the intruded media, and could be formulated by following equation:

$$K_\phi = \frac{2(1+\sin\phi)}{1-\sin\phi} e^{\pi\tan\phi} \int_0^1 \eta A(\eta,\phi)\mathrm{d}\eta \tag{27}$$

where $A(\eta,\phi)$ could be expressed as

$$A(\eta,\phi) = \left(\frac{r_1^{1+\tan^2\beta}}{r_2^{\tan^2\beta} r_3}\right)^{\sin\phi} e^{\sin\phi\tan\beta Z(\eta,\phi)} \tag{28}$$

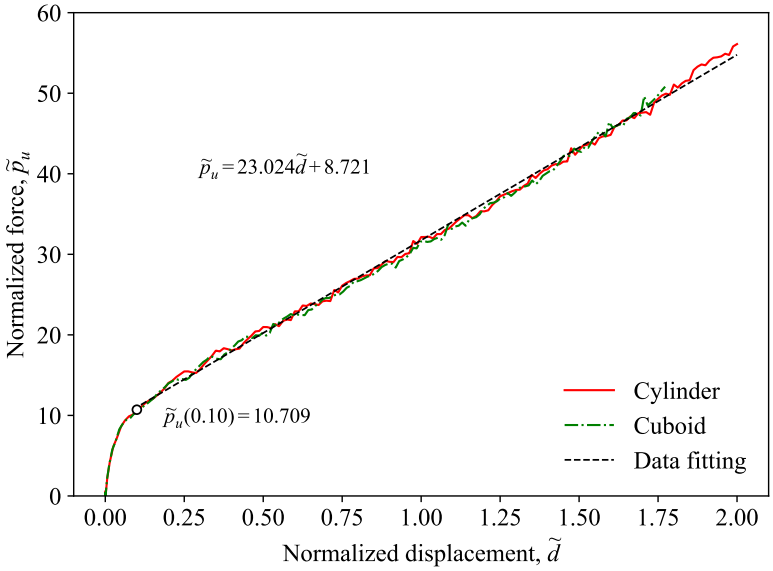

FIGURE 13 Normalized force versus normalized displacement

and coefficient β, r_1, r_2, r_3 and $Z(\eta, \phi)$ are computed as follows:

$$\beta = \frac{\pi}{4} - \frac{\phi}{2} \tag{29a}$$

$$r_1 = R\left(1 + \frac{2(1-\eta)}{\tan\beta} e^{\frac{\pi}{2}\tan\phi}\right) \tag{29b}$$

$$r_2 = R\left(1 + \frac{R(1-\eta)}{\tan\beta} e^{\frac{\pi}{2}\tan\phi}\right) \tag{29c}$$

$$r_3 = R\eta \tag{29d}$$

$$Z(\eta, \phi) = \int_0^{\pi/2} \frac{(\eta - 1)e^{\psi\tan\phi}\cos(\psi + \beta)}{\cos\phi[\sin\beta + (1-\eta)e^{\psi\tan\phi}\sin(\psi - \beta)]} \mathrm{d}\psi \tag{29e}$$

In an attempt to further compare our numerical solution with the above theoretical prediction, the repose angle ϕ of the RVE packings is measured as 26.8° with a standard deviation is 1.5. We plot (ϕ, K_ϕ) from current multiscale modeling onto Fig. 14 in a comparison with the theoretical prediction[55] and experimental data[55,56,58]. It is clear that our multiscale solution is in an excellent agreement with the prediction by the modified Archimedes' law, providing another strong support for this newly proposed theory from a numerical perspective beyond a pure DEM study[57].

In addition to the $K_\phi - \phi$ relation, the modified Archimedes' law also implies that the resistant force during the intrusion into a granular matter is linearly proportional to the effective penetrating volume $V(d) = Sd + V_{sz}(d)$ that comprises the immersed volume of the intruder Sd and the growing volume of the stagnant zone $V_{sz}(d)$. Specifically, the latter governs the initial nonlinear regime of the resistance force. To date, the growing mechanism of the stagnant zone remains open.[58] postulates that the stagnant zone extends its volume from a flat disc to a cone wedge, analogous to a fixed-base frustum with increasing height. On the other hand,[59] argued that the stagnant zone starts as a short wedge and gradually 'fanning out', converging eventually to a trapezoid-like shape. Therefore, it is of interest to investigate the initial nonlinear regime of force-displacement curve and its underlying development mechanism for the stagnant zone.

A critical step of investigating the development mechanism of stagnant zone is to select an appropriate quantity to measure the stagnant zone. As pointed out in[55,58], the formation of stagnant zone is largely attributed to the jamming of grain particles ahead of the flat plate, and the material close to the side surface of the stagnant zone would fall into plastic flow regime, showing a strong tendency of shearing. From the particle-scale perspective, shearing commonly takes the form of particle rolling, and therefore, the averaged particle angular velocity $\dot{\theta}$ (obtained via $\dot{\theta} = (\theta^{t+1} - \theta^t)/\Delta t$, where θ represents the averaged particle

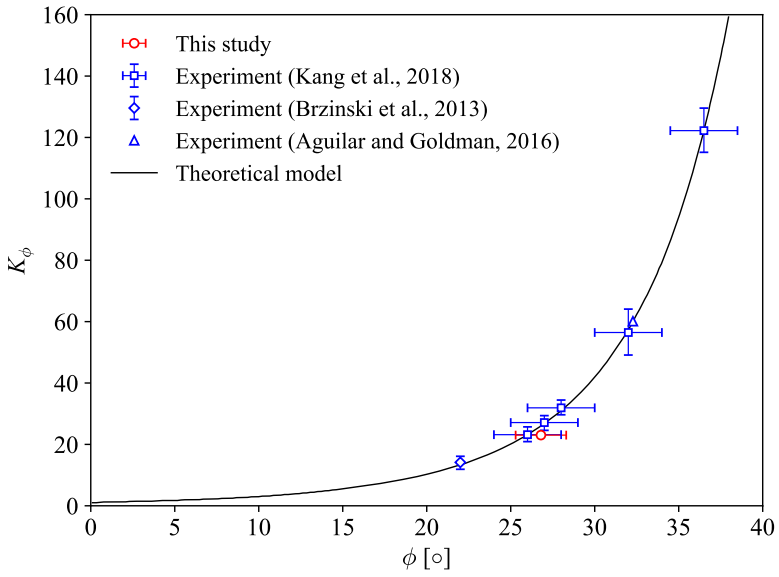

FIGURE 14 Relation of K_ϕ and ϕ

rotation as indicated in Eqn.15) serves as an ideal indicator for visualizing the dynamic development of the stagnant zone. Fig. 15 compares the averaged particle angular velocity for the cylindrical intruder in various stages of the intrusion. Those for the cuboid intruder show similar patterns and are not presented here for brevity. It is observed that a stagnant zone is formed in front of the intruder, being partitioned by those with noticeable averaged particle angular velocity. In particular, during the initial period of intrusion (Fig. 15 a-d), the stagnant zone takes a shape of frustum whose base is coincident with the bottom of the intruder. As the intrusion proceeds, the height of the frustum gradually increases, and at $\widetilde{d} = 0.10$, the frustum eventually develops into a cone and maintains its shape afterward till the end of the intrusion at $\widetilde{d} = 2.0$. This observation is in line with the postulation by[58], while the 'fanning out' mechanism of the wedge[59] has not been observed from our simulations.

The DEM solutions at particle scale enable us to further examine the complex evolution of stagnant zone. In Fig. 16 , we show the contact force chain network for three probing RVEs at different stages during the formation of the stagnant zone. As marked in Fig. 11 c, the three selected RVEs [1] are located underneath the center of the intruder with varying depths (and indeed they are eventually enclosed within the final stagnant zone). Before the commencement of the intrusion, the RVE buried deeper has a slightly stronger contact force because of the larger geo-static pressure. Shortly after the intrusion (*i.e.*, $d = 0.007m$), the RVE on the top is firstly compacted while the other two do not experience noticeable compression. As the penetration continues (*i.e.*, $d = 0.0437m$), the compression propagates to the intermediate RVE while leaving the bottom RVE roughly intact. The evolution of the force chain in Fig. 16 clearly reveals the propagation of the compaction during the intrusion process, which is previously reported in high-porosity sandstones[22,23]. Again, this mesoscopic analysis further confirms the postulation by[58] that the stagnant zone forms in the mechanism of growing frustum whose height keeps increasing due to the downward solidification.

5 | CONCLUSIONS

This study presents a scalable three-dimensional (3D) multiscale framework for continuum-discrete modeling of granular media. The proposed multiscale framework rigorously couples Material Point Method (MPM) and Discrete Element Method (DEM) for cross-scale simulation of large-scale boundary value problems. The MPM is used to solve the governing equations of a macroscopic boundary value problem that may enter a large deformation regime, while the DEM serves as a surrogate model for the continuum history-dependent constitutive response at each material point of MPM. The innovative bridging of MPM

[1] coordinates for RVEs: (0.0156, 0.0156, 4.86), (0.0156, 0.0156, 4.80), (0.0156, 0.0156, 4.70)

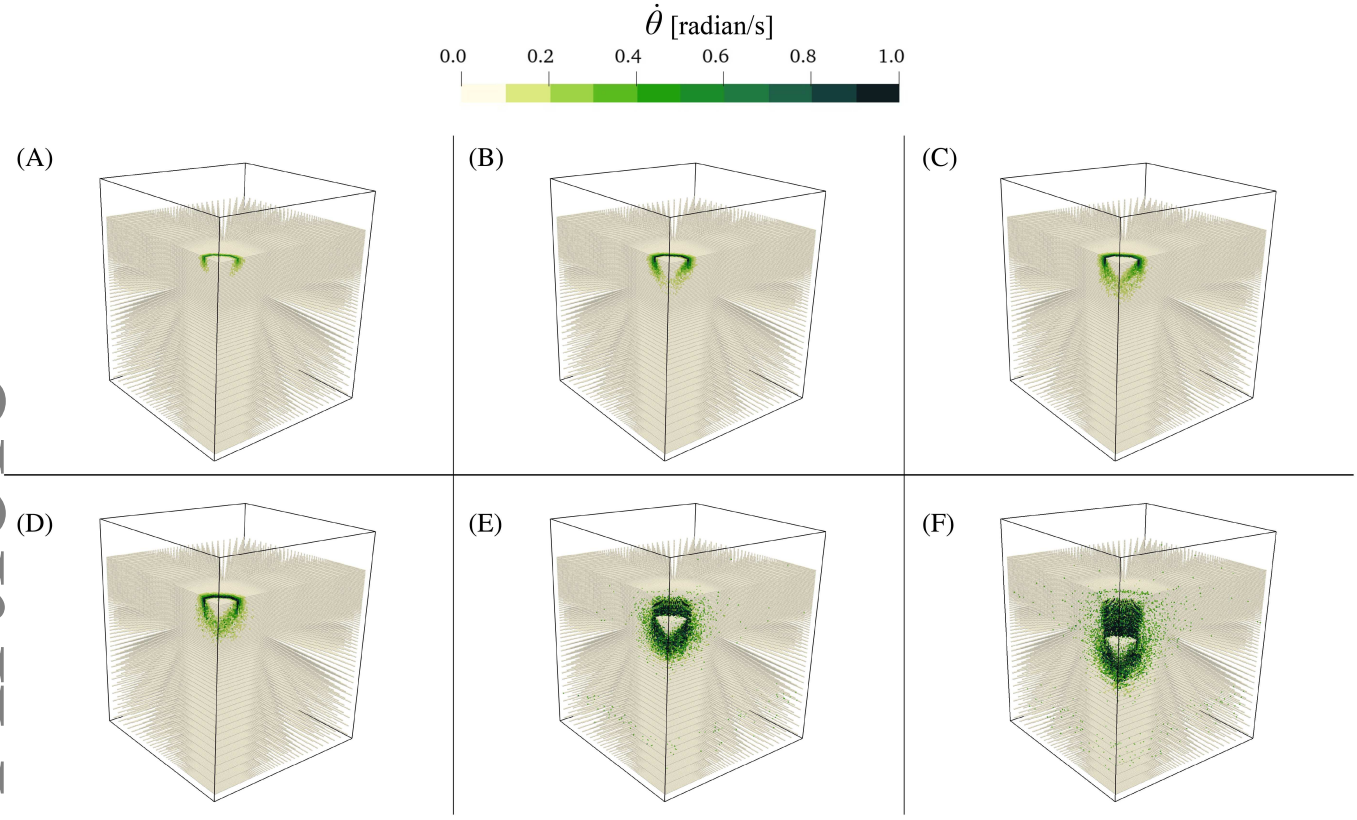

FIGURE 15 Averaged particle angular velocity magnitude $\dot{\theta}$ for the cylindrical intruder in various stages of the penetration: (a) $\widetilde{d} = 0.0062$, (b) $\widetilde{d} = 0.025$, (c) $\widetilde{d} = 0.050$ (d) $\widetilde{d} = 0.10$, (e) $\widetilde{d} = 1.0$ and (b) $\widetilde{d} = 2.0$

and DEM allows us to easily tackle geomechanical problems characterized by large deformation and strain localization while respecting their grain-scale physics. The major findings are summarized as follows:

1. The proposed multiscale framework has been well validated by unit element tests and its application to modeling 3D granular column collapse. The multiscale model offers consistent predictions with pure DEM simulations of the used RVE for the unit element test and comparable data with experimental tests on the column collapse problem.

2. To accommodate the high computation cost pertaining to 3D multiscale simulations, an effective and scalable parallel scheme has been propoised based on the *flat MPI* model. Through loading and shearing individual RVE in a specified MPI process, task parallelism and data parallelism are achieved. It is demonstrated that parallel scheme could achieve around 32X and 40X speedup in strong and weak scaling tests, respectively.

3. A large-scale complex intruder problem is simulated by our proposed multiscale approach empowered by the parallelism schemes. It is found that the resistant force and penetration depth relation during the intrusion exhibits an initial non-linear response before becoming linear, and the slope of the steady-state response K_ϕ depends only on the internal friction of the intruded granular media, providing a strong numerical support for the recently proposed modified Archimedes' law theory[55]. Further cross-scale analyses also reveal that the stagnant zone develops downwards from the top, following a frustum shape with a fixed base and an increasing height.

Although the parallel scheme based on the *flat MPI* model eases the implementation and helps to achieve excellent numerical performance for the proposed multiscale approach, it is suitable only for moderate resources (MPI process number $\sim \mathcal{O}(10^3)$) and problem size (RVE number $\sim \mathcal{O}(10^6)$). When both sizes of nodes and the problem dimension increase, the communication overhead and the MPM cost gradually grow and become the bottleneck of the entire computational framework, affecting its overarching performance. It deserves further investigations on the overall parallelism to gain better performance. This may include the implementation of multiple CPU-based[60] or GPU-based[61,62] parallelism for the MPM solver and optimization of the communication overhead for massively large scaling.

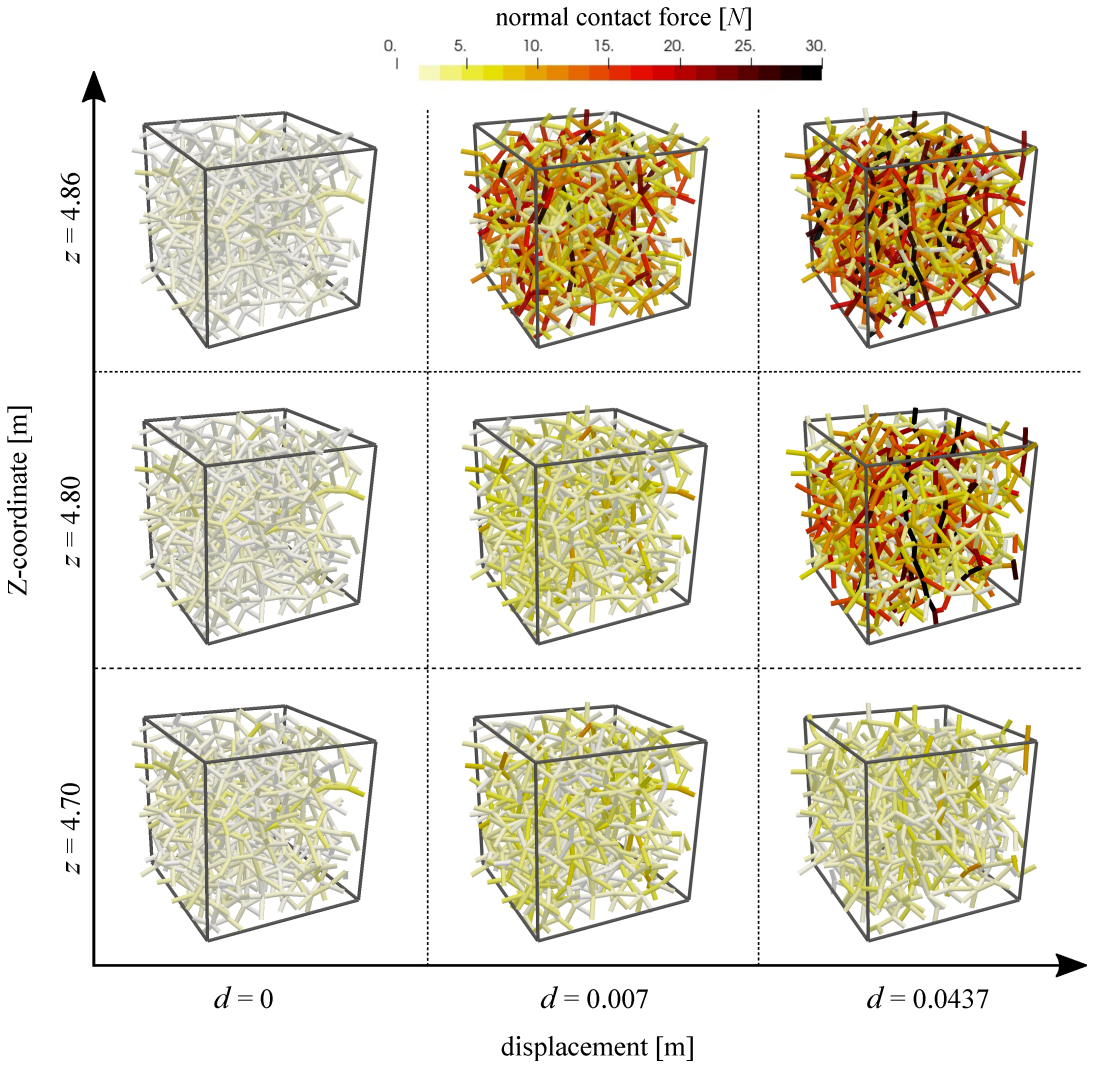

FIGURE 16 The evolution of force chains for three selected RVEs

Some modeling issues related the multiscale approach itself are also noteworthy. Because of large deformation or strain localization, it is observed that some attached RVEs to the material points (e.g., inside shear band) deform severely, becoming excessively thin and slender to require a reinitialization. This treatment unavoidably results in the loss of material loading history and introduces inaccuracy to some extends. It is noted that some effort have been make recently to address such issue, for example, using a rotating framework of reference and developing an adaptive RVE with evolutionary periodic boundary [63,64,65]. It would be encouraging to incorporate these attempts into the proposed approach to further advance the multiscale modeling of granular media.

ACKNOWLEDGMENTS

This work was financially supported by the National Natural Science Foundation of China (by Project No. 51909095 and No. 11972030), Research Grants Council of Hong Kong (by GRF Project No. 16211221), the Guangdong Basic and Applied Basic Research Foundation (2020A1515011525). JZ acknowledges the sponsorship of Ministry of Education on his 'Chang Jiang Scholar Chair Professorship' with Wuhan University. Any opinions, findings, and conclusions or recommendations expressed in this material are those of the authors and do not necessarily reflect the views of the financial bodies.

DATA AVAILABILITY STATEMENT

Some or all data, models, or code that support the findings of this study are available from the corresponding author upon reasonable request.

References

1. Bolton MD. The Strength and Dilatancy of Sands. *Géotechnique* 1986; 36(1): 65–78. doi: 10.1680/geot.1986.36.1.65
2. Schofield AN, Wroth CP. *Critical State Soil Mechanics*. New York: McGraw-Hill London . 1968.
3. Borja RI, Andrade JE. Critical State Plasticity. Part VI: Meso-scale Finite Element Simulation of Strain Localization in Discrete Granular Materials. *Computer Methods in Applied Mechanics and Engineering* 2006; 195(37): 5115–5140. doi: 10.1016/j.cma.2005.08.020
4. Zhao J, Guo N. Unique Critical State Characteristics in Granular Media Considering Fabric Anisotropy. *Géotechnique* 2013; 63(8): 695–704. doi: 10.1680/geot.12.P.040
5. Li XS, Dafalias YF. Anisotropic Critical State Theory: Role of Fabric. *Journal of Engineering Mechanics* 2012; 138(3): 263–275. doi: 10.1061/(ASCE)EM.1943-7889.0000324
6. Gao Z, Zhao J. Strain Localization and Fabric Evolution in Sand. *International Journal of Solids and Structures* 2013; 50(22-23): 3634–3648. doi: 10.1016/j.ijsolstr.2013.07.005
7. Gaume J, Gast T, Teran J, van Herwijnen A, Jiang C. Dynamic Anticrack Propagation in Snow. *Nature Communications* 2018; 9(1): 3047. doi: 10.1038/s41467-018-05181-w
8. Stomakhin A, Schroeder C, Chai L, Teran J, Selle A. A Material Point Method for Snow Simulation. *ACM Transactions on Graphics* 2013; 32(4): 1. doi: 10.1145/2461912.2461948
9. Askari H, Kamrin K. Intrusion Rheology in Grains and Other Flowable Materials. *Nature Materials* 2016; 15(12): 1274–1279. doi: 10.1038/nmat4727
10. Agarwal S, Karsai A, Goldman DI, Kamrin K. Surprising Simplicity in the Modeling of Dynamic Granular Intrusion. *Science Advances* 2021; 7(17): eabe0631. doi: 10.1126/sciadv.abe0631
11. Li WL, Guo N, Yang ZX, Helfer T. Large-Deformation Geomechanical Problems Studied by a Shear-Transformation-Zone Model Using the Material Point Method. *Computers and Geotechnics* 2021; 135: 104153. doi: 10.1016/j.compgeo.2021.104153
12. Fu P, Dafalias YF. Study of Anisotropic Shear Strength of Granular Materials Using DEM Simulation. *International Journal for Numerical and Analytical Methods in Geomechanics* 2011; 35(10): 1098–1126. doi: 10.1002/nag.945
13. Guo N, Zhao J. The Signature of Shear-Induced Anisotropy in Granular Media. *Computers and Geotechnics* 2013; 47: 1–15. doi: 10.1016/j.compgeo.2012.07.002
14. Wei J, Wang G. Evolution of Fabric Anisotropy in Cyclic Liquefaction of Sands. *Journal of Micromechanics and Molecular Physics* 2016; 01(03n04): 1640005. doi: 10.1142/S2424913016400051
15. Liang W, Zhao J. Multiscale Modeling of Large Deformation in Geomechanics. *International Journal for Numerical and Analytical Methods in Geomechanics* 2019; 43(5): 1080–1114. doi: 10.1002/nag.2921
16. Guo N, Zhao J. A Coupled FEM/DEM Approach for Hierarchical Multiscale Modelling of Granular Media. *International Journal for Numerical Methods in Engineering* 2014; 99(11): 789–818. doi: 10.1002/nme.4702
17. Desrues J, Argilaga A, Caillerie D, et al. From Discrete to Continuum Modelling of Boundary Value Problems in Geomechanics: An Integrated FEM-DEM Approach. *International Journal for Numerical and Analytical Methods in Geomechanics* 2019; 43(5): 919–955. doi: 10.1002/nag.2914

18. Liu Y, Sun W, Yuan Z, Fish J. A Nonlocal Multiscale Discrete-Continuum Model for Predicting Mechanical Behavior of Granular Materials. *International Journal for Numerical Methods in Engineering* 2016; 106(2): 129–160. doi: 10.1002/nme.5139

19. Wang K, Sun W. A Semi-Implicit Discrete-Continuum Coupling Method for Porous Media Based on the Effective Stress Principle at Finite Strain. *Computer Methods in Applied Mechanics and Engineering* 2016; 304: 546–583. doi: 10.1016/j.cma.2016.02.020

20. Zhao S, Zhao J, Lai Y. Multiscale Modeling of Thermo-Mechanical Responses of Granular Materials: A Hierarchical Continuum–Discrete Coupling Approach. *Computer Methods in Applied Mechanics and Engineering* 2020; 367: 113100. doi: 10.1016/j.cma.2020.113100

21. Guo N, Chen LF, Yang ZX. Multiscale Modelling and Analysis of Footing Resting on an Anisotropic Sand. *Géotechnique* 2021: 1–13. doi: 10.1680/jgeot.20.P.306

22. Wu H, Papazoglou A, Viggiani G, Dano C, Zhao J. Compaction Bands in Tuffeau de Maastricht: Insights from X-ray Tomography and Multiscale Modeling. *Acta Geotechnica* 2020; 15(1): 39–55. doi: 10.1007/s11440-019-00904-9

23. Wu H, Zhao J, Liang W. Pattern Transitions of Localized Deformation in High-Porosity Sandstones: Insights from Multiscale Analysis. *Computers and Geotechnics* 2020; 126: 103733. doi: 10.1016/j.compgeo.2020.103733

24. Wu H, Zhao J, Liang W. The Signature of Deformation Bands in Porous Sandstones. *Rock Mechanics and Rock Engineering* 2020; 53(7): 3133–3147. doi: 10.1007/s00603-020-02100-8

25. Liang W, Zhao J, Wu H, Soga K. Multiscale Modeling of Anchor Pullout in Sand. *Journal of Geotechnical and Geoenvironmental Engineering* 2021.

26. Liang W, Zhao S, Wu H, Zhao J. Bearing Capacity and Failure of Footing on Anisotropic Soil: A Multiscale Perspective. *Computers and Geotechnics* 2021; 137: 104279. doi: 10.1016/j.compgeo.2021.104279

27. Mitchell JK, Soga K, others . *Fundamentals of Soil Behavior*. 3. John Wiley & Sons New York . 2005.

28. Guo N, Zhao J. 3D Multiscale Modeling of Strain Localization in Granular Media. *Computers and Geotechnics* 2016; 80: 360–372. doi: 10.1016/j.compgeo.2016.01.020

29. Xu X, Jin F, Sun Q, Soga K, Zhou GG. Three-Dimensional Material Point Method Modeling of Runout Behavior of the Hongshiyan Landslide. *Canadian Geotechnical Journal* 2018; 56(9): 1318–1337. doi: 10.1139/cgj-2017-0638

30. Li X, Sovilla B, Jiang C, Gaume J. Three-Dimensional and Real-Scale Modeling of Flow Regimes in Dense Snow Avalanches. *Landslides* 2021. doi: 10.1007/s10346-021-01692-8

31. Bardenhagen SG, Kober EM. The Generalized Interpolation Material Point Method. *Computer Modeling in Engineering and Sciences* 2004; 5(6): 477–496.

32. Mindlin RD, Deresiewicz H. Elastic Spheres in Contact under Varying Oblique Forces. *J. Applied Mech.* 1953; 20: 327–344.

33. Yimsiri S, Soga K. Micromechanics-Based Stress–Strain Behaviour of Soils at Small Strains. *Géotechnique* 2000; 50(5): 559–571. doi: 10.1680/geot.2000.50.5.559

34. Zhao S, Evans TM, Zhou X. Effects of Curvature-Related DEM Contact Model on the Macro- and Micro-Mechanical Behaviours of Granular Soils. *Géotechnique* 2018; 68(12): 1085–1098. doi: 10.1680/jgeot.17.P.158

35. Christoffersen J, Mehrabadi MM, Nemat-Nasser S. A Micromechanical Description of Granular Material Behavior. *Journal of Applied Mechanics* 1981; 48(2): 339. doi: 10.1115/1.3157619

36. Nicot F, Hadda N, Guessasma M, Fortin J, Millet O. On the Definition of the Stress Tensor in Granular Media. *International Journal of Solids and Structures* 2013; 50(14-15): 2508–2517. doi: 10.1016/j.ijsolstr.2013.04.001

37. Kumar K, Salmond J, Kularathna S, et al. Scalable and Modular Material Point Method for Large-Scale Simulations. *arXiv:1909.13380* 2019.

38. Kularathna S, Liang W, Zhao T, Chandra B, Zhao J, Soga K. A Semi-Implicit Material Point Method Based on Fractional-Step Method for Saturated Soil. *International Journal for Numerical and Analytical Methods in Geomechanics* 2021. doi: 10.1002/nag.3207

39. Smilauer V, Catalano E, Chareyre B, et al. *Yade Documentation 2nd Ed*. Zenodo . 2015

40. Zhao S, Zhao J. SudoDEM: Unleashing the Predictive Power of the Discrete Element Method on Simulation for Non-Spherical Granular Particles. *Computer Physics Communications* 2021; 259: 107670. doi: 10.1016/j.cpc.2020.107670

41. Pheatt C. Intel® Threading Building Blocks. *Journal of Computing Sciences in Colleges* 2008; 23(4): 298.

42. Nakajima K. Parallel Iterative Solvers of GeoFEM with Selective Blocking Preconditioning for Nonlinear Contact Problems on the Earth Simulator. In: IEEE. ; 2003: 13–13

43. Nakajima K. Three-Level Hybrid vs. Flat MPI on the Earth Simulator: Parallel Iterative Solvers for Finite-Element Method. *Applied Numerical Mathematics* 2005; 54(2): 237–255. doi: 10.1016/j.apnum.2004.09.025

44. Dagum L, Menon R. OpenMP: An Industry Standard API for Shared-Memory Programming. *IEEE computational science and engineering* 1998; 5(1): 46–55.

45. Lube G, Huppert HE, Sparks RSJ, Hallworth MA. Axisymmetric Collapses of Granular Columns. *Journal of Fluid Mechanics* 2004; 508: 175–199. doi: 10.1017/S0022112004009036

46. Lajeunesse E, Monnier JB, Homsy GM. Granular Slumping on a Horizontal Surface. *Physics of Fluids* 2005; 17(10): 103302. doi: 10.1063/1.2087687

47. Bui HH, Fukagawa R, Sako K, Ohno S. Lagrangian Meshfree Particles Method (SPH) for Large Deformation and Failure Flows of Geomaterial Using Elastic–Plastic Soil Constitutive Model. *International Journal for Numerical and Analytical Methods in Geomechanics* 2008; 32(12): 1537–1570. doi: 10.1002/nag.688

48. Chandra B, Singer V, Teschemacher T, Wüchner R, Larese A. Nonconforming Dirichlet Boundary Conditions in Implicit Material Point Method by Means of Penalty Augmentation. *Acta Geotechnica* 2021. doi: 10.1007/s11440-020-01123-3

49. Szewc K. Smoothed Particle Hydrodynamics Modeling of Granular Column Collapse. *Granular Matter* 2016; 19(1): 3. doi: 10.1007/s10035-016-0684-3

50. Fern EJ, Soga K. The Role of Constitutive Models in MPM Simulations of Granular Column Collapses. *Acta Geotechnica* 2016; 11(3): 659–678. doi: 10.1007/s11440-016-0436-x

51. Amdahl GM. Validity of the Single Processor Approach to Achieving Large Scale Computing Capabilities. In: AFIPS. ; 1967: 483–485.

52. Zhao S, Zhao J, Liang W. A Thread-Block-Wise Computational Framework for Large-Scale Hierarchical Continuum-Discrete Modeling of Granular Media. *International Journal for Numerical Methods in Engineering* 2021; 122(2): 579–608. doi: 10.1002/nme.6549

53. Kollet SJ, Maxwell RM, Woodward CS, et al. Proof of Concept of Regional Scale Hydrologic Simulations at Hydrologic Resolution Utilizing Massively Parallel Computer Resources. *Water Resources Research* 2010; 46(4). doi: 10.1029/2009WR008730

54. Gustafson JL. Reevaluating Amdahl's Law. *Communications of the ACM* 1988; 31(5): 532–533.

55. Kang W, Feng Y, Liu C, Blumenfeld R. Archimedes' Law Explains Penetration of Solids into Granular Media. *Nature Communications* 2018; 9(1): 1101. doi: 10.1038/s41467-018-03344-3

56. Brzinski TA, Mayor P, Durian DJ. Depth-Dependent Resistance of Granular Media to Vertical Penetration. *Physical Review Letters* 2013; 111(16): 168002. doi: 10.1103/PhysRevLett.111.168002

57. Feng Y, Blumenfeld R, Liu C. Support of Modified Archimedes' Law Theory in Granular Media. *Soft matter* 2019; 15(14): 3008–3017.

58. Aguilar J, Goldman DI. Robophysical Study of Jumping Dynamics on Granular Media. *Nature Physics* 2016; 12(3): 278–283. doi: 10.1038/nphys3568

59. Agarwal S, Karsai A, Goldman DI, Kamrin K. Efficacy of Simple Continuum Models for Diverse Granular Intrusions. *Soft Matter* 2021; 17(30): 7196–7209. doi: 10.1039/D1SM00130B

60. Fang Y, Li M, Gao M, Jiang C. Silly Rubber: An Implicit Material Point Method for Simulating Non-Equilibrated Viscoelastic and Elastoplastic Solids. *ACM Transactions on Graphics* 2019; 38(4): 118:1–118:13. doi: 10.1145/3306346.3322968

61. Dong Y, Grabe J. Large Scale Parallelisation of the Material Point Method with Multiple GPUs. *Computers and Geotechnics* 2018; 101: 149–158. doi: 10.1016/j.compgeo.2018.04.001

62. Wang X, Qiu Y, Slattery SR, et al. A Massively Parallel and Scalable Multi-Gpu Material Point Method. *ACM Transactions on Graphics* 2020; 39(4).

63. Qu T, Feng Y, Wang M. An Adaptive Granular Representative Volume Element Model with an Evolutionary Periodic Boundary for Hierarchical Multiscale Analysis. *International Journal for Numerical Methods in Engineering* 2021; n/a(n/a). doi: 10.1002/nme.6620

64. Dhakal TR, Zhang DZ. Combining Dual Domain Material Point Method with Molecular Dynamics for Thermodynamic Nonequilibriums. *Journal of Computational Physics* 2018; 374: 984–995. doi: 10.1016/j.jcp.2018.08.007

65. Wang M, Zhang DZ. Deformation Accommodating Periodic Computational Domain for a Uniform Velocity Gradient. *Computer Methods in Applied Mechanics and Engineering* 2021; 374: 113607. doi: 10.1016/j.cma.2020.113607